Hindawi
Advances in Materials Science and Engineering
Volume 2022, Article ID 3817050, 11 pages
https://doi.org/10.1155/2022/3817050

Research Article

Hydrothermal Synthesis and Photocatalytic Properties of Graphene@Ag/$AgSb_2O_{5.8}$ Composites: Reaction Laws of the Composites in Sintering Process

Haomei Liu,[1] **Xihai Hao**,[1] **Yuejun Liu**,[1] **and Aiguo Yan**[2]

[1]*College of Packaging and Materials Engineering, Hunan University of Technology, Zhuzhou 412000, China*
[2]*School of Materials Science and Engineering, Xiamen University of Technology, Xiamen 361024, China*

Correspondence should be addressed to Yuejun Liu; yjliu_2005@126.com and Aiguo Yan; 754601094@qq.com

Received 26 September 2021; Revised 30 December 2021; Accepted 17 January 2022; Published 3 February 2022

Academic Editor: Zhigang Zang

Copyright © 2022 Haomei Liu et al. This is an open access article distributed under the Creative Commons Attribution License, which permits unrestricted use, distribution, and reproduction in any medium, provided the original work is properly cited.

Single-phase silver antimonite have quite low oxidation and reduction potential because of the easy recombination of photogenerated electrons and holes. In the study, a novel ternary graphene@Ag/$AgSb_2O_{5.8}$ (G @Ag/ASO) visible-light-driven photocatalyst was successfully synthesized by a simple hydrothermal method. The morphology, structure, and chemical composition of G @Ag/ASO and its sinters at different temperatures in the air atmosphere were systematically characterized by a range of techniques. Reaction laws of the composites in the sintering process have been revealed based on the Ellingham diagram. The photocatalytic degradation of rhodamine B (RhB) dye and tetracycline hydrochloride (OTC-HCl) by the as-synthesized photocatalyst was investigated under visible light irradiation. The G@Ag/ASO-500 (the sinter at 500°C) exhibits degradation efficiency of 80% for RhB and 85% for OTC-HCl in 120 min, higher than those for $AgSb_2O_{5.8}$ (20% and 24%, respectively). The graphene-enhanced Ag-loaded $AgSb_2O_{5.8}$ model is proposed and reasonably accounts for the high-efficiency electron-hole transfer mechanism through four contact potentials and the crucial role of graphene sheets on the surface of the composites. The present study provides a new perspective for enhancing photocatalytic performance.

1. Introduction

The widespread use of antibiotics (e.g. tetracycline hydrochloride) in aquaculture, human medical care, and animal husbandry has caused serious water pollution [1, 2]. In order to efficiently destruct these organic molecules from the aquatic environment, various techniques, including adsorption, electrochemistry, and catalysis have been developed. Among those advanced oxidation processes (AOPs), semiconductor-mediated piezo-photocatalysis [3–5] and photocatalysis [6–18], which possess strong redox potentials to produce high reactive radicals of O_2^- and $OH^·$, have been proven to be one of the most reliable technologies in water purification by virtue of their eco-friendly, cost-effective, and high-efficiency characteristics.

In recent years, silver antimonite photocatalysis has been developed as a promising "green" photocatalyst with visible light sensitivity in environmental remediation in which the pollutant molecules are converted into nontoxic inorganic molecules by their reaction with both the reactive radicals O_2^- and OH [19, 20]. In order to efficiently destruct molecules of pollutants, photocatalysis must possess strong redox potentials to produce high reactive radicals of O_2^- and OH [21]. However, the single-phase silver antimonite have quite low oxidation and reduction potential and suffer from the easy recombination of photogenerated electrons and holes [22]. Combining two semiconductors to construct silver antimonite-based heterostructures photocatalysts such as $AgSbO_3/NaNbO_3$ [23, 24], $AgSbO_3/AgNbO_3$ [25] or designing a "Z-scheme" such as $AgSbO_3/Ag/g\text{-}C_3N_4$ [21], have been considered to be efficient methods to prepare photocatalysts possessing stronger reduction and oxidation potentials.

In contrast to the above heterostructures photocatalysts, visible-light-triggered plasmonic photocatalysts have been

recognized as another promising alternative to the traditional single-phase photocatalysts [26, 27]. Recently, it has been reported that many binary semiconductors modified by nanosized metals like Ag enhance the overall photocatalytic efficiency due to its unique surface plasmon resonance (SPR) features originating from the collective oscillations of the electrons on the surface of the Ag nanoparticles (NPS) at the range of visible light [28, 29]. In these binary Ag-semiconductor composites, metal Ag NPS can absorb visible light and facilitate the separation of e_{CB}^- and h_{VB}^- generated on the semiconductor and improve the photocatalytic efficiency of these composites.

Graphene (G), a 2D single or more layers of sp^2-hybridized carbon atoms with a large $\pi - \pi$ conjugation on the surface, has attracted great attention due to its extraordinary physical properties including superior charge transport, unique optical properties, high thermal conductivity, large theoretical specific surface area, and good mechanical strength [30, 31]. Tremendous efforts have been made for coupling graphene with other semiconductors to synthesis binary heterojunction photocatalysts with improved photocatalytic activity [32, 33]. The ultrahigh electron conductivity of graphene resulted from the large $\pi - \pi$ conjugation upon the surface, allows the follow of electrons from the semiconductor to its surface, assuring efficient electron-hole separation. Moreover, the potential of most of the photocatalyst are normally higher than graphene/graphene$^-$ (−0.08 V vs standard hydrogen electrode (SHE), pH = 0) and then enabling the fast electron migration from the photocatalyst to the graphene [34].

Herein, we firstly successfully manufactured a ternary photocatalytic composite graphene@Ag/$AgSb_2O_{5.8}$ (G@Ag/ASO) composed of $AgSb_2O_{5.8}$ (ASO), Ag, and more-layers graphene (G) via a simple one-step hydrothermal method, and then the ternary samples were sintered under an air atmosphere at different temperatures. Reaction laws of metal Ag and graphene in the composites in the sintering process based on the Ellingham diagram were investigated. The photocatalytic activity of the ternary structure was studied by measuring the degradation of RhB and OTC-HCl. The experimental results show that the as-prepared ternary photocatalysts of G@Ag/ASO hybrids exhibit excellent photocatalytic activity in the visible light irradiation. The electron-hole transfer mechanism of the ternary G@Ag/ASO is discussed based on the graphene-enhanced metal-loaded semiconductor model.

2. Experimental Sections

2.1. Materials. Potassium pyroantimonite ($KSbO_6H_6$) and $AgNO_3$ were purchased from Xilong Scientific Co., Ltd. (China). Graphene was obtained from Xiamen Kaina Graphene Technology Co., Ltd. All chemical reagents are analytic grade without further purifying. Deionized water was prepared with ultrapure water of 18.2 MΩ (Milli-Q, Millipore).

2.2. Preparation of G@Ag/ASO Composites. Firstly, 0.1 g graphene powder was dispersed in 70.0 mL deionized water kept ultrasonic station at 40°C for 1.5 h. Then 1.051 g (4.00 mmol) $KSbO_6H_6$ was slowly added into the above mixture under stirring at 80°C for 0.5 h. Secondly, 0.7136 g (4.2 mmol) of $AgNO_3$ was dissolved in 10.0 mL deionized water and slowly added into the above mixture and then kept stirring for 5 minutes. Thirdly, the mixture (pH value is 6.8 measured using a pH meter) was sealed in a Teflon-lined stainless-steel autoclave (100 ml capacity) and heated at 120°C for 24 h. After the reaction, the autoclave was cooled down to room temperature naturally. After washing (with deionized water and 99.5% ethanol) and drying (at 80°C for 10 h), the sample of G@Ag/ASO was obtained.

In order to investigate the effect of temperature on the structure, composition, and photocatalytic activity of the composites, the samples were sintered under an air atmosphere at temperatures of 250°C, 500°C, and 750°C for 3h with the rate of 2°C/min, and the as-annealed samples were labeled as G@Ag/ASO-250, G@Ag/ASO-500, and G@Ag/ASO-750, respectively.

As a comparison, silver antimonate was also prepared by a hydrothermal route like our previous reports [35].

2.3. Characterization. The obtained samples were characterized on a Bruker D8 advanced X-ray powder diffractometer (XRD) with Cu Kα radiation ($\lambda = 1.5418$ Å). The size and morphology of the as-synthesized products were determined by a Zeiss Gemini 500 scanning electron microscope (SEM). High-resolution transmission electron microscopy (HRTEM) images were collected by JEOL JEM 2010. The chemical state of samples was investigated by X-ray photoelectron spin (XPS). UV-visible diffuse reflectance spectra were obtained on the Shimadzu UV-2600 spectrophotometer. Electron spin resonance (ESR) signals of the samples were investigated by a Bruker E580 spectrometer.

The photocatalytic activity was estimated by the photocatalytic degradation of both RhB and OTC-HCl under visible light ($\lambda \geq 420$ nm) irradiation from a 300-W Xe lamp with a cutoff filter (L-42). The distance between the light source of the 300-W Xe lamp and the surface of the solution is 10 cm. The concentration of RhB or OTC-HCl was determined by measuring the absorbance at a wavelength of about 554 nm. 0.05 g powder sample was suspended in a 100 ml RhB (4.0 mg/L) or OTC-HCl (16 mg/L) aqueous solution and then dark reaction for 30 min under continuous stirring of the suspension solution to get the absorption equilibrium before light illumination. At a given time interval, 4.0 ml of the suspension was taken as a sample and filtered to measure the concentration of RhB or OTC-HCl solution by monitoring the intensity at maximum absorption wavelength from a UV-visible spectrophotometer.

3. Results and Discussion

The formation process of G@Ag/ASO is schematically illustrated in Figure 1. Firstly, lots of tiny $AgSb_2O_{5.8}$ crystal nuclei are formed by the reaction (equation (1)) between $S_bO_6H_6^-$ (dissociated from potassium pyroantimonate) and Ag^+ (dissociated from silver nitrate) and preferentially

adsorb on the interface on the graphene. Some Ag crystal nuclei can be reduced from Ag^+ in a hydrothermal reaction system (equation (2)) [35] and gather on the surface of $AgSb_2O_{5.8}$ particles. Both were aged in a Teflon-lined stainless-steel autoclave after stirring and aging.

$$SbO_6H_6^- + Ag^+ \longrightarrow AgSb_2O_{5.8}\downarrow, \quad (1)$$

$$H_2 + 2Ag^+ = 2Ag + 2H^+. \quad (2)$$

Typical XRD patterns for graphene and G@Ag/ASO are displayed in Figure 2(a). The characteristic peak of as-prepared G@Ag/ASO appears at approximately 26.26 degrees from graphene and the other diffraction peaks are consistent well with JPCDS card No.00-052-0263 of $AgSb_2O_{5.8}$. The XRD peak of the metallic Ag is not observed, which may be due to the amount of Ag nanoparticles being too low to be detected by XRD [36]. Figure 2(b) presents the typical SEM image of G@Ag/ASO, in which the large quantity and good uniformity of $AgSb_2O_{5.8}$ hollow nanoparticles (many broken cavities can be seen) and some smaller particles dispersing on the surface of the hollow nanoparticles can be clearly observed. All of these particles gather on the surface of the 2D layer of graphene to be combined into the ternaryG@Ag/ASO composite. Figure 2(c) shows the TEM image of the same sample and it can be observed that particles with the different shapes and sizes are suspended on the surface or encased in transparent graphene films, the size of the larger particle is ~110 nm and the smaller one is about 10 nm. Some smaller particles are anchored on the surface of the bigger particles. Figure 2(d) presents an HRTEM image for G@Ag/ASO composite and shows that there are the crystal lattice 0.30 nm identical with (222) of $AgSb_2O_{5.8}$ for a bigger particle, 0.23 nm with (111) of metal Ag for a smaller one, and 0.34 nm for graphene with 24-layer. The results show that the ternary G@Ag/ASO sample composed of $AgSb_2O_{5.8}$, metal Ag, and 24-layer graphene has been synthesized via a simple hydrothermal route.

In order to investigate the effect of temperature on the structure, composition, and photocatalytic activity of the G@Ag/ASO composites, the powder was sintered under an air atmosphere at 250°C, 500°C, and 750°C, respectively. Figure 3(a) shows an SEM image of the sample of G@Ag/ASO-250 (annealed at 250°C) and clearly reveals that large hollow hexagon-type nanoparticles with the size of ~130 nm either gather on the surface of graphene sheet or are encased in graphene films (intact layered structure). Some smaller particles with the size of about 30 nm are embedded on the surface on the larger particles. When the annealing temperature was increased from 250°C to 500°C and further up to 750°C, the multilayer-structure graphene sheet begins to break up (SEM image of G@Ag/ASO-500 shown in Figure 3(b)) and even disappear (SEM image of G@Ag/ASO-750 in Figure 3(c)), which means that the multilayer-structure graphene would be consumed to broken and thinned and finally wear out with the temperature increases.

Typical XRD patterns for pure silver antimonite, the samples "a" (identified as G@Ag/ASO-250), "b" (G@Ag/ASO-500), and "c" (G@Ag/ASO-750) are displayed in Figure 3(d), respectively. In the bottom, all diffraction peaks of the individual phase of silver antimonite are also consistent well with JPCDS card No.00-052-0263 of $AgSb_2O_{5.8}$. For the samples "a" and "b", both of them are composed of $AgSb_2O_{5.8}$ and graphene. But, the intensity of the characteristic peak of 26.26 degrees of sample "b" is weaker than one of "a," reflecting the decreases of graphene content of sample "b." All diffraction peaks of the sample "c" are the same as the $AgSb_2O_{5.8}$ sample without the peak of 26.26 degrees, which means the content of graphene is too low to be detected by XRD. The XRD peaks of metallic Ag are also not observed, but the thermodynamics research and results from the Ellingham diagram [37], commonly used in the field of metallurgy, proves that metallic silver still exists in the calcined systems. In the calcined systems, the possible chemical reactions and their accordingly variation values of the standard molar Gibbs free energy $\Delta_r G^{\theta}_m$ (298K) [38] at room temperature (298K) can be represented as follows:

$$2Ag\,(s) + \frac{1}{2}O_2\,(g) = Ag_2O\,(s) \quad \Delta_r G^{\Theta}_{m,3}\,(298K) = -11.20kJ \bullet mol^{-1}, \quad (3)$$

$$C\,(\text{graphene}) + O_2\,(g) = CO_2\,(g) \quad \Delta_r G^{\Theta}_{m,4}\,(298K) = -394.36kJ \bullet mol^{-1}, \quad (4)$$

$$CO\,(g) + \frac{1}{2}O_2\,(g) = CO_2\,(g) \quad \Delta_r G^{\Theta}_{m,5}\,(298K) = -257.19kJ \bullet mol^{-1}, \quad (5)$$

$$C\,(\text{graphene}) + \frac{1}{2}O_2\,(g) = CO\,(g) \quad \Delta_r G^{\Theta}_{m,6}\,(298K) = -137.17kJ \bullet mol^{-1}. \quad (6)$$

According to the equation of $(\partial(\Delta_r G^{\Theta}_m)/\partial T)_P = -\Delta_r S^{\Theta}_m$, the value of $\Delta_r G^{\Theta}_{m,4}$ changes very little with temperature because the variation values of the standard molar entropy ($\Delta_r S^{\Theta}_{m,4}$) are almost zero resulting from the same stoichiometry of the gaseous substance before and after the reaction (4). The value of $\Delta_r G^{\Theta}_{m,5}$ will decrease with increasing temperature due to the increasing $\Delta_r S^{\Theta}_{m,3}$ in consequence of the increased number (+0.5 mol) of gas

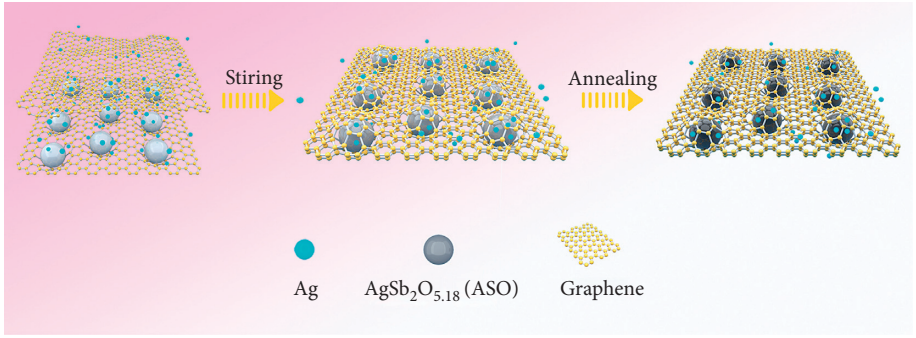

Figure 1: Schematic illustration for the formation process of G@Ag/ASO composite. The $AgSb_2O_{5.8}$ and Ag nucleus grow and anchor onto the surface of graphene to form into G@Ag/ASO composite.

molecules in reaction 5 when the reaction progress is 1 mol ($\xi = 1$ mol). In the same way, the values of $\Delta_r G^{\Theta}_{m,3}$ and $\Delta_r G^{\Theta}_{m,6}$ will increase with increasing temperature because of the decreased number (-0.5 mol) of gas molecules in the reaction 3 and 6, respectively. The curves describing how the value of $\Delta_r G^{\Theta}_m$ varies with temperature are shown in Figure 4 (Ellingham diagram). The detailed calculation process can be found in the supplementary part.

In the calcined systems, silver oxide (Ag_2O) may be reduced by reducing agents C(graphene) and/or newly formed carbon monoxide (CO), thermochemical reactions equation is as follows:

$$Ag_2O(s) + \frac{1}{2}C(\text{graphene}) = 2Ag(s) + \frac{1}{2}CO_2(g) \quad \Delta_r G^{\Theta}_{m,7} = \Delta_r G^{\Theta}_{m,4} - \Delta_r G^{\Theta}_{m,3}, \tag{7}$$

$$Ag_2O(s) + C(\text{graphene}) = 2Ag(s) + CO(g) \quad \Delta_r G^{\Theta}_{m,8} = \Delta_r G^{\Theta}_{m,5} - \Delta_r G^{\Theta}_{m,3}, \tag{8}$$

$$Ag_2O(s) + CO = 2Ag(s) + CO_2(g) \quad \Delta_r G^{\Theta}_{m,} = \Delta_r G^{\Theta}_{m,6} - \Delta_r G^{\Theta}_{m,3}. \tag{9}$$

When the value of $\Delta_r G^{\Theta}_m$ of the reaction is less than zero, this means that the Ag_2O can be reduced to metallic silver. As can be seen from the Ellingham diagram, the curve position for Ag_2O (reaction 3) is always below the curve positions for reactions 4, 5, and 6 in the range of 298–1200K, indicating that the values of $\Delta_r G^{\Theta}_{m,7}$, $\Delta_r G^{\Theta}_{m,8,}$ and $\Delta_r G^{\Theta}_{m,9}$ are less than zero and Ag_2O can easily be reduced to silver by C (graphene) and/or CO in the range of 298–1200K. In other words, metallic Ag in the as-fabricated G@Ag/ASO cannot be reversed into Ag_2O when the annealing temperature is in the range of 298–1200K.

Thermodynamic studies have also revealed the laws of thermodynamics and kinetics of C (graphene) in calcination systems. As shown in Figure 4, both of $\Delta_r G^{\Theta}_{m,4}$ and $\Delta_r G^{\Theta}_{m,6}$ are less than -394.36 and -137.17 kJ·mol^{-1} in the range of 298–1200K, respectively, far less than zero, means that graphene can be easily converted into carbon dioxide (CO_2) and CO, which is not consistent with the real experimental results. Our own experimental evidence has led us to believe that the reactions of C (graphene) with oxygen form CO_2 and CO which are controlled by the reaction rate. When the temperature increases from 298K to 773K and further to 1023K, the reaction rate rapidly increased and resulted in partial consumption and finally the layers of graphene disappear.

The surface chemical state and bonding configuration of $AgSb_2O_{5.8}$ and G@Ag/ASO composite were investigated by XPS. As shown in Figure 5(a), the peak for C 1s only for G@Ag/ASO is around 284.4 eV, which may be attributed to sp^2-hybridized carbons over graphene. The O 1s XPS is illustrated in Figure 5(b). The fitted two apparent peaks at around 529.8 eV and 530.5 eV over both $AgSb_2O_{5.8}$ and G@Ag/ASO correspond to crystal lattice oxygen of $AgSb_2O_{5.8}$ and the surface chemisorbed hydroxyl, respectively [22]. The XPS spectrum for Ag 3d at 367.4 eV and 373.4 eV over $AgSb_2O_{5.8}$ are assigned to Ag^+ whereas the peaks at around 367.7 eV and 373.7 eV correspond to Ag^0 (Figure 5(c)), suggesting the existence of metallic Ag [39]. All peaks of Ag 3d of G@Ag/ASO shift to a slightly larger binding energy compared with $AgSb_2O_{5.8}$, revealing a smaller electron density on Ag in G@Ag/ASO because of the bonding effect [40]. The Sb 3d XPS spectra over $AgSb_2O_{5.8}$ are composed of fitted peaks at around 529.8 eV and 531.0 eV and a single peak at 539.2 eV (see in Figure 5(d)). These peaks can be assigned to antimony bounded to sliver and oxygen in the form of Sb^{3+} and Sb^{5+} oxidation states [41]. The Sb 3d peaks over G@Ag/ASO have no shift when $AgSb_2O_{5.8}$ was composited into G@Ag/ASO, suggesting that the electron cloud may be unchanged on Sb in G@Ag/ASO.

Figure 6(a) displays the UV-vis absorption spectrum of the as-synthesized samples. The absorption edge of $AgSb_2O_{5.8}$ is at about 430 nm (Curves 6a). The ternary graphene-enhanced composites, including G@Ag/ASO (curve 6b), G@Ag/ASO-250 (curve 6c), and G@Ag/ASO-

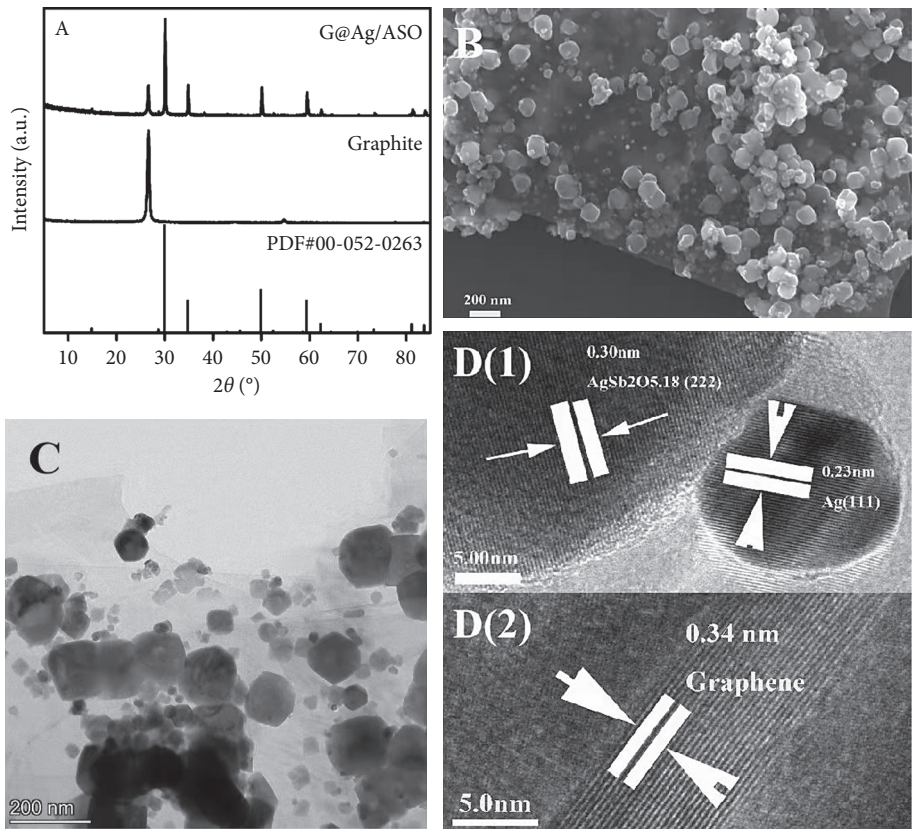

Figure 2: (a) X-ray diffraction (XRD) pattern, (b) SEM, (c) TEM, and (d) HRTEM images of G@Ag/ASO composite.

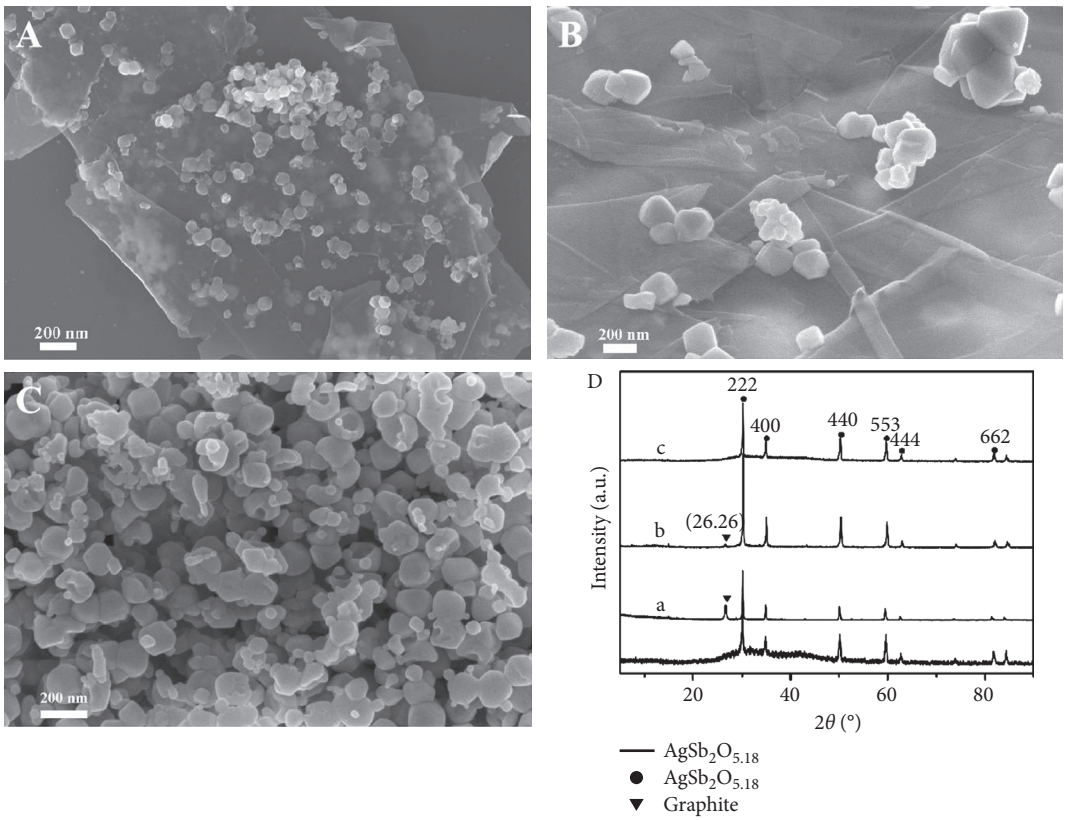

Figure 3: SEM images of (a) G@Ag/ASO-250, (b) G@Ag/ASO-500, and (c) G@Ag/ASO-750; (d) XRD patterns of the different composites: (A) G@Ag/ASO-250; (B) G@Ag/ASO-500; (C) G@Ag/ASO-750.

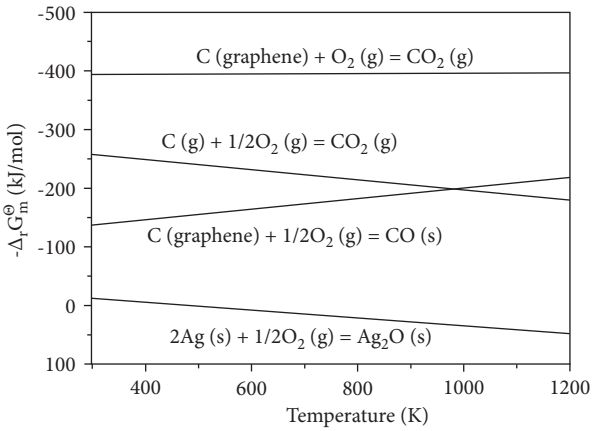

Figure 4: Ellingham diagram.

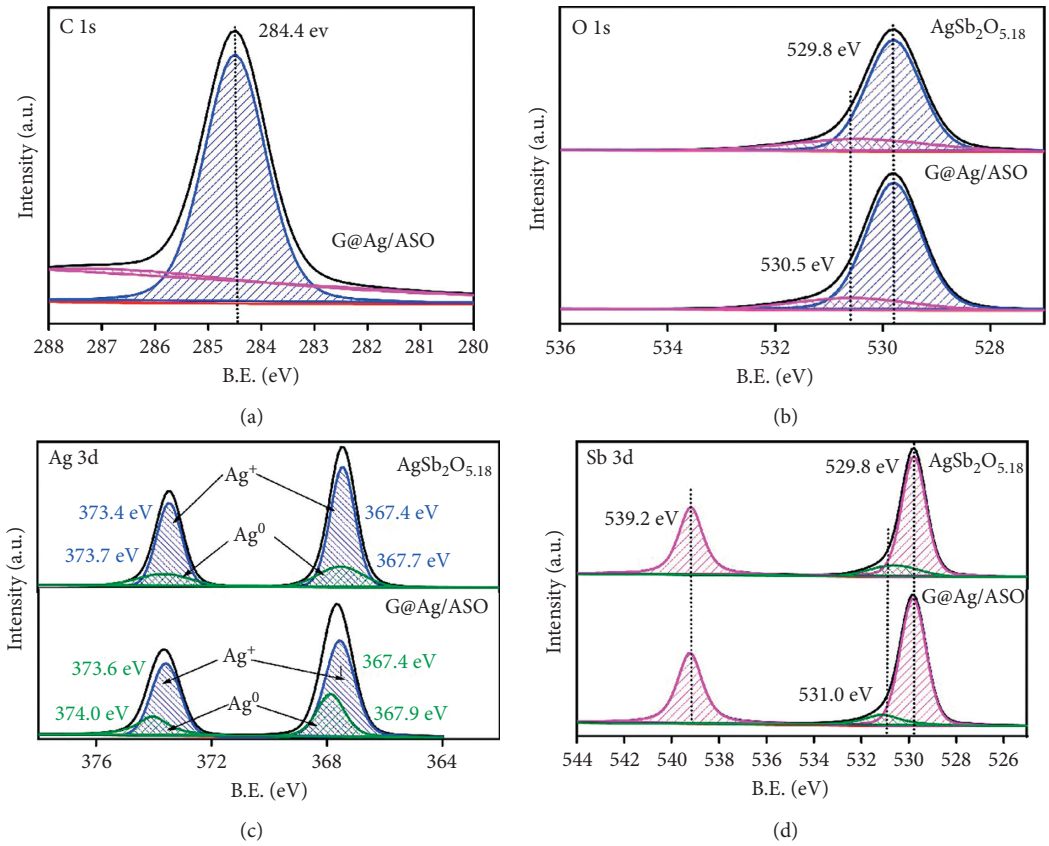

Figure 5: XPS spectrum of (a) C 1s, (b) Ag 3d, (c) O 1s, and (d) Sb 3d for both of $AgSb_2O_{5.8}$ and G@Ag/ASO.

500 (curve 6d) exhibit a broad background absorption in the wide range of ultraviolet and visible wavelengths ($\lambda > 240$ nm), which can be attributed to the 0 eV bandgap of graphene [42]. Figure 6(b) shows the DRS spectra and bandgaps calculation diagram of $AgSb_2O_{5.8}$. On the account that silver antimonite is an indirect bandgap semiconductor, the calculated apparent energy bandgap (Eg) of the $AgSb_2O_{5.8}$ is 2.68 eV.

According to the formula (10)

$$\alpha h\upsilon = A\left(h\upsilon - E_g\right)^{1/2}, \tag{10}$$

where E_g, h, α, υ, and A are bandgap, plank constant, absorption coefficient, light frequency, and constant, respectively.

The 5,5-dimethyl-1-pyrroline-N-oxide (DMPO) was employed to confirm the generation of active species O_2^- and $OH^\cdot$ by an ESR spin trap. Figure 7(a) exhibits ESR signal of DMPO-O_2^- for $AgSb_2O_{5.8}$, G@Ag/ASO.

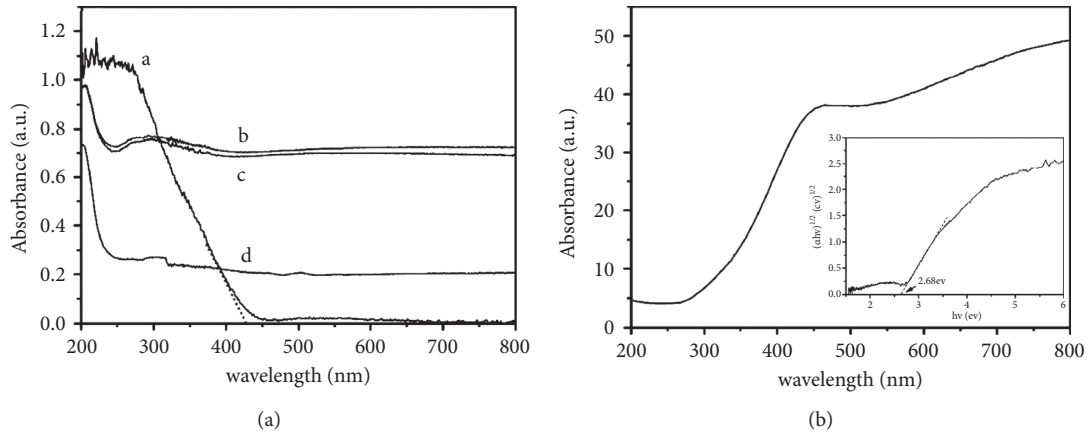

Figure 6: (a) UV-vis light adsorption of the different composites: (A) $AgSb_2O_{5.8}$, (B) G@Ag/ASO, (C) G@Ag/ASO-250, (D) G@Ag/ASO-500; (b) UV-vis DRS and bandgaps calculation diagram of $AgSb_2O_{5.8}$.

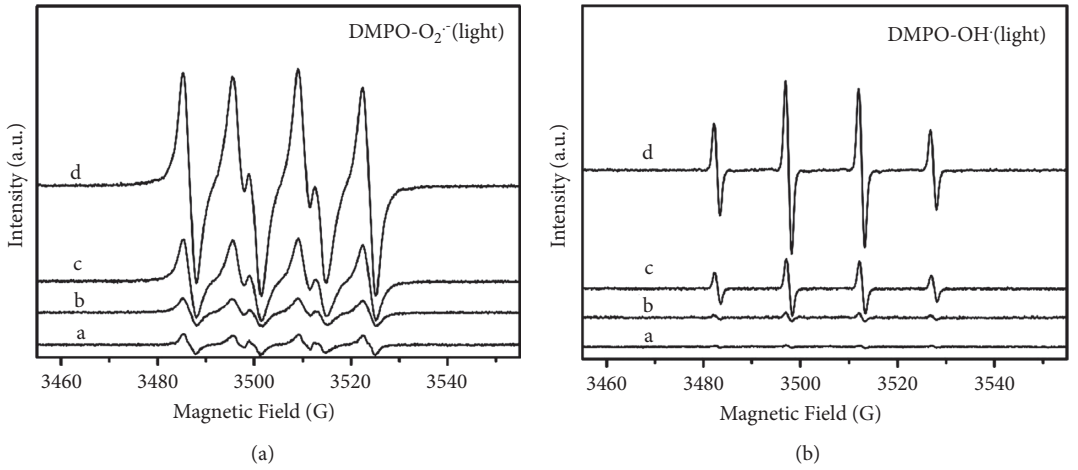

Figure 7: ESR signals of (a) DMPO-O_2^- and (b) DMPO-OH· for (A)$AgSb_2O_{5.8}$; (B)G@Ag/ASO; (C) G@Ag/ASO-250; (D) G@Ag/ASO-500.

G@Ag/ASO-250 and G@Ag/ASO-500 composites under visible light irradiation, respectively. The results show that there are obvious signals of DMPO-O_2^-at the magnetic field of 3486, 3495, 3499, 3509, 3513, and 3523G for all of the samples, indicating that all of the as-synthesized materials have a reduction potential to produce O_2^-. But the intensities of signals for the different materials are a little different. Compared to pure $AgSb_2O_{5.8}$, the ternary composites exhibit stronger intensities of the signal of DMPO-O_2^-, meaning that reduction ability is enhanced when $AgSb_2O_{5.8}$ semiconductor has been loaded with silver particles and graphene membranes. The G@Ag/ASO-500 composite with broken and thinned graphene exhibits stronger signal intensities than other graphene-based composites, which may be due to the larger specific surface area of G@Ag/ASO-500 than those of other graphene-based composites with more layers and intact graphene. Usually, the increase of the specific surface area leads to the improvement of photocatalytic activity. On the other hand, the G@Ag/ASO-500 composite also exhibits much higher signal intensity than $AgSb_2O_{5.8}$ and other graphene-based composites to produce DMPO-OH (Figure 7(b)). There is a little signal for $AgSb_2O_{5.8}$, suggesting that the oxidation potential is too low to produce OH. The oxidization reaction to generate OH· thus happens on the active site of graphene in graphene-based composites.

Visible-light-induced photodegradation of rhodamine B (RhB) was selected as model reaction to evaluate the photocatalytic properties of the different graphene-based samples. As a comparison, RhB degradation with pure $AgSb_2O_{5.8}$ was also carried out under identical conditions. As shown in Figure 8(a), about 7% of RhB in the solution was destructed in 120 min under visible light irradiation ($\lambda > 420$ nm) without a photocatalyst. 20% of RhB was destructed within 120 min over $AgSb_2O_{5.8}$. The G@Ag/ASO-500 displays much enhanced photocatalytic performance compared to $AgSb_2O_{5.8}$ because that 80% RhB was removed by G@Ag/ASO-500 in 120 min. The linear relationship between ln (1/A) and t (min) of the as-prepared samples was shown in Figure 8(b), which confirms that the photodegradation reaction of this study is indeed pseudo-first-order and the rate equation (6) is as follows:where k_1 and R

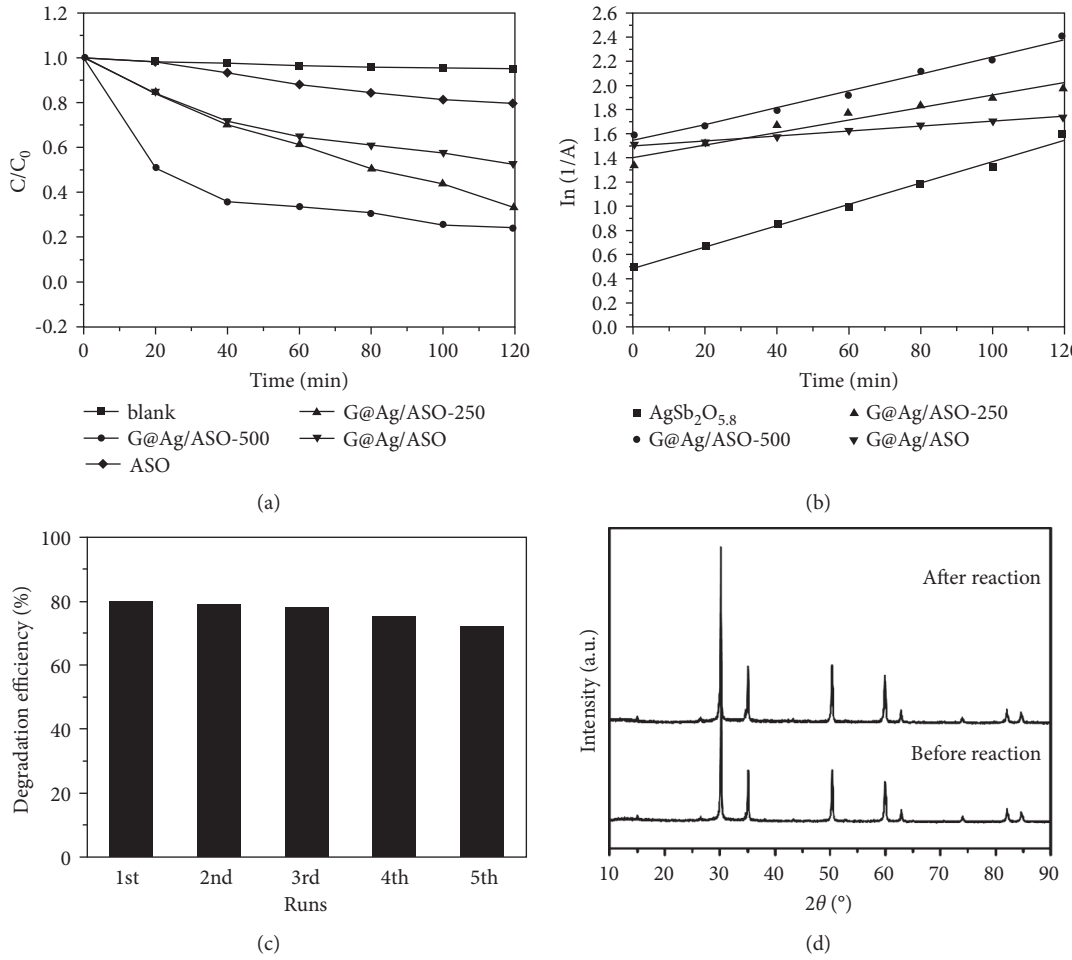

Figure 8: (a) photocatalytic degradation of RhB and (b) linear transform ln (1/A) of the kinetic curves of RhB degradation; (c) five recycling runs of G@Ag/ASO-500 for RhB removal; (d) the XRD patterns of the original and recycled G@Ag/ASO-500.

are apparent reaction rate constant and constant, respectively. According to Equation (6) and Figure 8(b), the values of k_1 of the photodegradation of RhB are $0.50\,\text{min}^{-1}$, $1.50\,\text{min}^{-1}$, $1.4\,\text{min}^{-1}$, and $1.58\,\text{min}^{-1}$ for $AgSb_2O_{5.8}$, G@Ag/ASO-250, G@Ag/ASO, and G@Ag/ASO-500, respectively. It appears that the G@Ag/ASO-500 composite exhibit about 3 folds RhB degradation rate as $AgSb_2O_{5.8.}$ On account of the significance of stability and reusability for the pragmatic application of photocatalysts, cycling degradation of RhB over G@Ag/ASO-500 was further conducted. As shown in Figure 8(c), G@Ag/ASO-500 did not present significant deactivation, and approximately 72% of RhB could be degraded even in the fifth run. The slight deterioration in the photocatalytic activity probably stemmed from the unavoided loss of the catalyst in the experiment. Good stability of ternary composites was further verified via using the XRD technique. Clearly, the phase of the used G@Ag/ASO-500 was almost identical to that of the original one (Figure 8(d)). These findings disclosed that G@Ag/ASO belongs to a type of stable visible light-driven photocatalyst, which could be a potential candidate for actual organics degradation.

$$\ln\left(\frac{1}{A}\right) = k_1 t + R, \tag{11}$$

To further validate its strong photocatalytic activity, the degradation of tetracycline hydrochloride (OTC-HCl) over G@Ag/ASO-500 was further performed. As shown in Figure 9, after 120 min of visible light irradiation, about 85% of OTC-HCl was eliminated by G@Ag/ASO-500 (vs ~3%, blank and 24%, $AgSb_2O_{5.8}$), demonstrating its high photocatalytic capability for the removal of antibiotics in aquaculture.

Based on the abovementioned results, a possible graphene-enhanced metal-loaded semiconductor model and evolved electron-hole transfer mechanism of the ternary G@Ag/ASO are proposed. As shown in Figure 10, smaller Ag particles (labeled as Ag 1 and Ag 2 near VBM and CBM of ASO, respectively) are attached to the ASO particles, which are surrounded by graphene to form a ternary G@Ag/ASO composite. The composite consists of four interfaces, including the interface between Ag 1 particle and the graphene, Ag 1 and the VBM of ASO, Ag 2 and the CBM of ASO, and Ag 2 and the graphene.

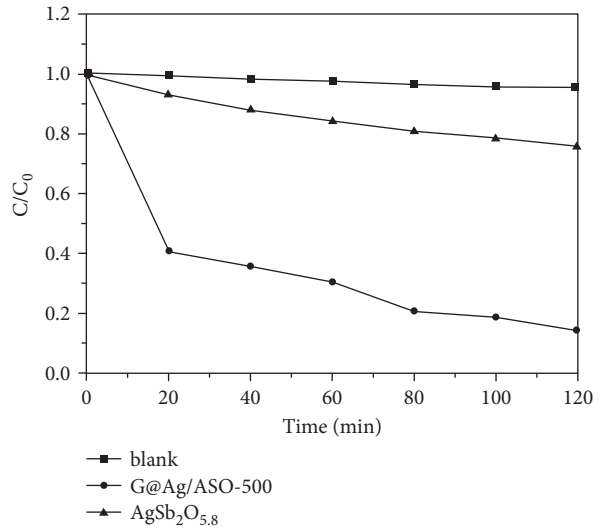

Figure 9: Photocatalytic degradation of OTC-HCl.

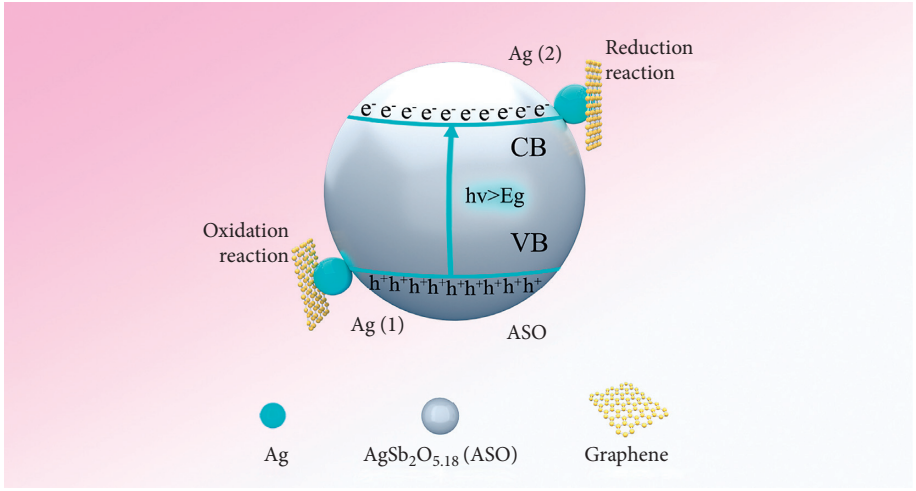

Figure 10: Model of charge separation proposed for G@Ag/ASO.

Under the irradiation of visible light, photoelectrons and holes are generated within the ASO semiconductor and form the internal potential $\psi_{VBM/CBM}$ between CBM (negative pole) and VBM (positive pole). The direction of $\psi_{VBM/CBM}$ is from CBM to VBM. Due to the localized surface plasmon resonance (LSPR) effect, plasmon-induced electron-hole pairs are also formed on the surface of Ag nanoparticles under visible light irradiation. As far as CBM of ASO is concerned, because of its close contact with metallic Ag 2 particle and the electrons excited to the CBM of ASO were entrapped by Ag 2 particle to recombine with the plasmon-induced holes through the Schottky barrier, a contact potential $\psi_{CBM/Ag(2)}$ is formed at the interface between CBM and Ag 2 particle. The direction of the $\psi_{Ag(2)/CBM}$ is from Ag(1) to CBM, which is the same as that of $\psi_{VBM/CBM.}$ Another contact potential $\psi_{G/Ag(2)}$ at the interface between Ag 2 particle and graphene is also formed because graphene has a delocalized conjugation electron cloud upon the surface and low potential graphene/graphene$^-$ (-0.08 eV vs SHE, pH = 0) [31] and enabling the fast electron migration from the Ag 2 particle (the potential Ag^+/Ag is +0.80 eV vs SHE, pH = 0) [43] to the graphene. The direction of the $\psi_{Ag(2)/G}$ is from graphene to Ag 2. The follow of electrons migration from CBM of ASO to Ag 2 particle and further to graphene assure efficient electron-hole separation of ASO semiconductor. Simultaneously, the electron migrated to the surface of graphene with strong reduction power can react with absorbed O_2 to produce O_2^-, which could oxidize the dye molecule of RhB or OTC-HCl and resulted in a high photocatalytic degradation rate. In the same way, the contact potential $\psi_{Ag(1)/VBM}$ at the interface between the VBM of ASO and Ag 1 particle (the direction is from VBM to Ag 1) and $\psi_{G/Ag(1)}$ between Ag 1 particle and graphene (the direction is from Ag 1 to graphene) are also formed. Both of $\psi_{Ag(1)/VBM}$ and $\psi_{G/Ag(1)}$ assure that the photogenerated holes migrate from the VBM of ASO to the surface of Ag1 particles and further to the surface of

graphene sheets. The holes that remain on the graphene can react with H_2O/OH^- to generate $OH^·$ with strong oxidizing power and directly oxidize the dye of RhB or OTC-HCl to CO_2, H_2O, and other micromolecules. Therefore, the graphene-enhanced Ag-loaded ASO model and evolved electron-hole transfer mechanism of the ternary G@Ag/ASO could reasonably explain the effective separation of the electron-hole pairs excited by ASO and resulted in enhanced photocatalytic activity. Because multilayer-structure graphene sheets in G@Ag/ASO were consumed to broken and thinned in calcining process, G@Ag/ASO-500 or G@Ag/ASO-250 possess larger specific surface area and more reaction sites than G@Ag/ASO. As a result, G@Ag/ASO-500 or G@Ag/ASO-250 exhibits stronger photocatalytic activity than G@Ag/ASO.

4. Conclusions

In summary, the ternary photocatalysts of G@Ag/ASO composites are successfully synthesized in the hydrothermal process and exhibited excellent photocatalytic activity for the decomposition of organic pollutants. The reaction laws of both metallic Ag and graphene in the annealing process have been revealed based on the Ellingham diagram. The graphene-enhanced Ag-loaded $AgSb_2O_{5.8}$ model is proposed and reasonably accounts for the high photocatalytic performance of G@Ag/ASO which possesses high efficiency of electron-hole pairs separation through four contact potentials. The graphene sheets on the surface of the composites play a crucial role. This novel ternary G@Ag/ASO composite may be a new potential material for environmental applications.

Data Availability

The data used to support the findings of this study are available from the corresponding author upon request.

Ethical Approval

This research was performed at the Hunan University of Technology and Xiamen University of Technology.

Conflicts of Interest

The authors declare that they have no conflicts of interest.

Authors' Contributions

Haomei Liu organized the research and wrote the manuscript, and Xihai Hao and Aiguo Yan provided the laboratory and apparatus. Yuejun Liu checked the manuscript and revised the manuscript according to the reviews' comments.

Acknowledgments

This research was funded by the National Natural Science Foundation of China (no.11872179).

Supplementary Materials

The detailed calculation process and additional Ref. can be found in the supplementary part. (*Supplementary Materials*)

References

[1] M. Qiao, G.-G. Ying, A. C. Singer, and Y.-G. Zhu, "Review of antibiotic resistance in China and its environment," *Environment International*, vol. 110, pp. 160–172, 2018.

[2] A. Karkman, T. T. Do, F. Walsh, and M. P. J. Virta, "Antibiotic-resistance genes in waste water," *Trends in Microbiology*, vol. 26, no. 3, pp. 220–228, 2018.

[3] S. C. Tu, Y. X. Guo, Y. H. Zhang et al., "Piezocatalysis and piezo-photocatalysis: catalysts classification and modification strategy, reaction mechanism, and practical application," *Advanced Functional Materials*, vol. 30, pp. 1–31, Article ID 2005158, 2020.

[4] X. Li, J. Wang, J. Zhang, C. Zhao, Y. Wu, and Y. He, "Cadmium sulfide modified zinc oxide heterojunction harvesting ultrasonic mechanical energy for efficient decomposition of dye wastewater," *Journal of Colloid and Interface Science*, vol. 607, pp. 412–422, 2022.

[5] Y. Li, H. F. Chen, L. K. Wang, T. T. Wu, Y. Wu, and Y. M. He, "$KNbO_3$/ZnO heterojunction harvesting ultrasonic mechanical energy and solar energy to efficiently degrade methyl orange," *Ultrasonics Sonochemistry*, vol. 78, pp. 1–10, Article ID 105754, 2021.

[6] S. J. Li, C. C. Wang, Y. P. Liu et al., "Photocatalytic degradation of antibiotics using a novel $Ag/Ag_2S/Bi_2MoO_6$ plasmonic p-n heterojunction photocatalyst: mineralization activity, degradation pathways and boosted charge separation mechanism," *Chemical Engineering Journal*, vol. 415, pp. 1–14, Article ID 128991, 2021.

[7] C. Wang, M. Cai, Y. Liu et al., "Facile construction of novel organic-inorganic tetra (4-carboxyphenyl) porphyrin/Bi2MoO6 heterojunction for tetracycline degradation: performance, degradation pathways, intermediate toxicity analysis and mechanism insight," *Journal of Colloid and Interface Science*, vol. 605, pp. 727–740, 2022.

[8] S. J. Li, C. C. Wang, Y. P. Liu et al., "Photocatalytic degradation of tetracycline antibiotic by a novel $Bi_2Sn_2O_7/Bi_2MoO_6$ S-scheme heterojunction: performance, mechanism insight and toxicity assessment," *Chemical Engineering Journal*, vol. 429, pp. 1–16, Article ID 132519, 2022.

[9] S. J. Li, B. Xue, J. L. Chen, W. Jiang, and Y. P. Liu, "BiOCOOH microflowers decorated with Ag/Ag_2CrO_4 nanoparticles as highly efficient photocatalyst for the treatment of toxic wastewater," *Catalysts*, vol. 10, no. 93, pp. 1–15, 2020.

[10] S. J. Li, J. L. Chen, S. W. Hu, H. l. Wang, W. Jiang, and X. B. Chen, "Facile construction of novel Bi_2WO_6/Ta_3N_5 Z-scheme heterojunction nanofibers for efficient degradation of harmful pharmaceutical pollutants," *Chemical Engineering Journal*, vol. 402, pp. 1–24, Article ID 126165, 2020.

[11] S. J. Li, C. C. Wang, M. J. Cai et al., "Facile fabrication of $TaON/Bi_2MoO_6$ core-shell S-scheme heterojunction nanofibers for boosting visible-light catalytic levofloxacin degradation and Cr(VI) reduction," *Chemical Engineering Journal*, vol. 428, pp. 1–15, Article ID 131158, 2022.

[12] S. Li, S. Hu, W. Jiang et al., "Facile synthesis of cerium oxide nanoparticles decorated flower-like bismuth molybdate for enhanced photocatalytic activity toward organic pollutant degradation," *Journal of Colloid and Interface Science*, vol. 530, pp. 171–178, 2018.

[13] S. J. Li, C. C. Wang, Y. P. Liu et al., "Facile preparation of a novel Bi_2WO_6/calcined mussel shell composite photocatalyst with enhanced photocatalytic performance," *Catalysts*, vol. 10, pp. 1–11, Article ID 1166, 2020.

[14] S. Li, S. Hu, W. Jiang, J. Zhang, K. Xu, and Z. Wang, "In situ construction of WO3 nanoparticles decorated Bi2MoO6 microspheres for boosting photocatalytic degradation of refractory pollutants," *Journal of Colloid and Interface Science*, vol. 556, pp. 335–344, 2019.

[15] S. Li, X. Shen, J. Liu, and L. Zhang, "Synthesis of Ta3N5/Bi2MoO6core-shell fiber-shaped heterojunctions as efficient and easily recyclable photocatalysts," *Environmental Sciences: Nano*, vol. 4, no. 5, pp. 1155–1167, 2017.

[16] X. Dai, L. Chen, Z. Li et al., "CuS/KTa0.75Nb0.25O3 nanocomposite utilizing solar and mechanical energy for catalytic N2 fixation," *Journal of Colloid and Interface Science*, vol. 603, pp. 220–232, 2021.

[17] Y. Ye, Z. Zang, T. Zhou et al., "Theoretical and experimental investigation of highly photocatalytic performance of CuInZnS nanoporous structure for removing the NO gas," *Journal of Catalysis*, vol. 357, pp. 100–107, 2018.

[18] L. Chen, X. Q. Dai, X. J. Li et al., "A novel Bi_2S_3/$KTa_{0.75}Nb_{0.25}O_3$ nanocomposite with high efficiency for photocatalytic and piezocatalytic N_2 fixation," *Journal. Materials. Chemical. A*, vol. 9, pp. 13344–13354, 2021.

[19] Z. Yi, J. Ye, N. Kikugawa et al., "An orthophosphate semiconductor with photooxidation properties under visible-light irradiation," *Nature Materials*, vol. 9, no. 7, pp. 559–564, 2010.

[20] T. Kako, N. Kikugawa, and J. Ye, "Photocatalytic activities of $AgSbO_3$ under visible light irradiation," *Catalysis Today*, vol. 131, no. 1, pp. 197–202, 2007.

[21] Z. Zheng, N. Zhang, T. Wang et al., "Ag1.69Sb2.27O6.25 coupled carbon nitride photocatalyst with high redox potential for efficient multifunctional environmental applications," *Applied Surface Science*, vol. 487, pp. 82–90, 2019.

[22] J. Shi, J. Ye, Q. Li et al., "Single-crystal nanosheet-based hierarchical AgSbO3with exposed {001} facets: topotactic synthesis and enhanced photocatalytic activity," *Chemistry - A European Journal*, vol. 18, no. 11, pp. 3157–3162, 2012.

[23] D. P. Chen, W. Bowers, and S. E. Skrabalak, "Aerosol-assisted combustion synthesis of single-crystalline NaSbO3 nanoplates: a topotactic template for ilmenite AgSbO3," *Chemistry of Materials*, vol. 27, no. 1, pp. 174–180, 2015.

[24] G. Li, W. Wang, N. Yang, and W. F. Zhang, "Composition dependence of AgSbO3/NaNbO3 composite on surface photovoltaic and visible-light photocatalytic properties," *Applied Physics A*, vol. 103, no. 1, pp. 251–256, 2011.

[25] G. Li, Y. Bai, W. F. Zhang, and H. Zhang, "Enhanced visible light photocatalytic properties of $AgNbO_3$/$AgSbO_3$ composites," *Materials Chemistry and Physics*, vol. 139, no. 2-3, pp. 1009–1013, 2013.

[26] M. A. Mahmoud, W. Qian, and M. A. El-Sayed, "Following charge separation on the nanoscale in Cu_2O-Au nanoframe hollow nanoparticles," *Nano Letters*, vol. 11, no. 1, pp. 3285–3289, 2011.

[27] T. Torimoto, H. Horibe, T. Kameyama et al., "Plasmon-enhanced photocatalytic activity of cadmium sulfide nanoparticle immobilized on silica-coated gold particles," *The Journal of Physical Chemistry Letters*, vol. 2, no. 16, pp. 2057–2062, 2011.

[28] D. B. Ingram, P. Christopher, J. L. Bauer, and S. Linic, "Predictive model for the design of plasmonic metal/semiconductor composite photocatalysts," *ACS Catalysis*, vol. 1, no. 10, pp. 1441–1447, 2011.

[29] M. M. Mohamed and K. S. Khairou, "Preparation and characterization of nanosilver/mesoporous titania photocatalysts for herbicide degradation," *Microporous and Mesoporous Materials*, vol. 142, no. 1, pp. 130–138, 2010.

[30] H. Wang, L. Zhang, Z. Chen et al., "Semiconductor heterojunction photocatalysts: design, construction, and photocatalytic performances," *Chemical Society Reviews*, vol. 43, no. 15, pp. 5234–5244, 2014.

[31] J. X. Low, J. Yu, M. Jaroniec, S. Wageh, and A. A. Al-Ghamdi, "Heterojunction photocatalysts," *Advanced Materials*, vol. 29, no. 1, pp. 1601694–1601714, 2017.

[32] Q. Xiang, J. Yu, and M. Jaroniec, "Graphene-based semiconductor photocatalysts," *Chemical Society Reviews*, vol. 41, no. 2, pp. 782–796, 2012.

[33] X. Huang, X. Qi, F. Boey, and H. Zhang, "Graphene-based composites," *Chemical Society Reviews*, vol. 41, no. 2, pp. 666–686, 2012.

[34] Q. Xiang, J. Yu, and M. Jaroniec, "Enhanced photocatalytic H2-production activity of graphene-modified titania nanosheets," *Nanoscale*, vol. 3, no. 9, pp. 3670–3678, 2011.

[35] H. M. Liu, X. H. Hao, Y. J. Liu, and A. G. Yan, "Hydrothermal preparation of $Ag/Ag_{1.69}Sb_{2.27}O_{6.25}$ sesame-hollow-ball-type nanocomposites: the Formation mechanism of metallic Ag in the Ag-H_2O system at 400 K," *Advances in Materials Science and Engineering*, vol. 2020, pp. 1582861–1582868, 2020.

[36] Y. Yang, W. Guo, Y. Guo, Y. Zhao, X. Yuan, and Y. Guo, "Fabrication of Z-scheme plasmonic photocatalyst Ag@AgBr/g-C3N4 with enhanced visible-light photocatalytic activity," *Journal of Hazardous Materials*, vol. 271, pp. 150–159, 2014.

[37] X. C. Fu, W. X. Shen, T. Y. Yao, and W. H. Hou, "Physical chemistry," *Higher Education Press*, vol. 1, pp. 361-362, 2005.

[38] X. C. Fu, W. X. Shen, T. Y. Yao, and W. H. Hou, "Physical chemistry," *Higher Education Press*, vol. 1, pp. 483–495, 2005.

[39] Y. Gong, X. Quan, H. Yu, and S. Chen, "Synthesis of Z-scheme Ag2CrO4/Ag/g-C3N4 composite with enhanced visible-light photocatalytic activity for 2,4-dichlorophenol degradation," *Applied Catalysis B: Environmental*, vol. 219, pp. 439–449, 2017.

[40] M. Ou, S. Wan, Q. Zhong et al., "Hierarchical Z-scheme photocatalyst of g-C3N4@Ag/BiVO4 (040) with enhanced visible-light-induced photocatalytic oxidation performance," *Applied Catalysis B: Environmental*, vol. 221, pp. 97–107, 2018.

[41] H. Wang, X. Yuan, H. Wang et al., "Facile synthesis of Sb2S3/ultrathin g-C3N4 sheets heterostructures embedded with g-C3N4 quantum dots with enhanced NIR-light photocatalytic performance," *Applied Catalysis B: Environmental*, vol. B193, pp. 36–46, 2016.

[42] J. Low, J. Yu, and W. Ho, "Graphene-based photocatalysts for CO2 reduction to solar fuel," *The Journal of Physical Chemistry Letters*, vol. 6, no. 21, pp. 4244–4251, 2015.

[43] X. C. Fu, W. X. Shen, T. Y. Yao, and W. H. Hou, "Physical chemistry," *Higher Education Press*, vol. 1, pp. 485-486, 2006.